Ocean Sci. Discuss., 8, 1575–1599, 2011
www.ocean-sci-discuss.net/8/1575/2011/
doi:10.5194/osd-8-1575-2011

Ocean Science Discussions

Eddy characteristics in the Northern South China Sea as inferred from Lagrangian drifter data

J. X. Li[1,2], **R. Zhang**[1,2], **and B. Jin**[1,2]

[1]Institute of Meteorology, PLA University of Science and Technology, Nanjing 211101, China
[2]PLA Research Center of Ocean Environment Numerical Simulation, Nanjing 211101, China

Received: 12 June 2011 – Accepted: 21 June 2011 – Published: 4 July 2011

Correspondence to: J. X. Li (lijiaxun2009@yahoo.com.cn)

Published by Copernicus Publications on behalf of the European Geosciences Union.

Abstract

Cyclones and anticyclones from large scale to submesoscale on the Northern South China Sea (NSCS) have been statistically characterized based on the satellite-tracked Lagrangian drifter data using a geometric eddy identification method. There are totally 1972 eddies identified, 4/5 of which are anticyclonic eddies. If the submesoscale eddies are eliminated, the other eddies in the NSCS will show a 1.1–1 dominance with the number (133) of anticyclones over the number (122) of cyclones. The spatial distribution of all the eddies are: in Zone Z1, the number of anticyclones dominate the number of cyclones, most of which are the submesoscale anticyclonic eddies with small radii; whereas, in Zone Z2, cyclonic eddies are a little more than anticyclonic eddies. The temporal distribution of eddy number in the NSCS has a close relation with monsoon. The number of the large eddies peaks during the winter monsoon, while they tend to decrease quickly in the transition periods of monsoon. In contrast, submesoscale eddies are likely to generate in the summer monsoon, which may be related to the baroclinic instability in the NSCS. The spatial and temporal patterns have a good agreement with the results of SSHA. The maximum and mean tangential velocities of anticyclones (cyclones) are 45 (30) cm s^{-1} and 30 (15) cm s^{-1}, respectively. Large scale eddies can be considered in geostrophic balance, but ageostrophic dynamics may be important for the submesoscale eddies where centrifugal effects cannot be ignored in the NSCS.

1 Introduction

The South China Sea (SCS) is the largest semi-closed marginal sea in the Western Pacific Ocean, connecting in the north with the Pacific through the deep Luzon Strait (depth > 2000 m) and with the East China Sea through the shallow Taiwan Strait (depth < 200 m), and in the south with Sulu and Java Seas through a number of shallow passages (Fig. 1). The surface area of the SCS is about 3.5 million square kilometers, with a mean depth of 1800 m and a maximum depth of 5400 m.

OSD
8, 1575–1599, 2011

The patterns of the whole SCS upper circulation are related to the Asia monsoon, with significant impact of Kuroshio on the northern part of circulation through Luzon Strait (Qu, 2000). In winter, the general circulation in the SCS is cyclonic gyre, while in summer, there is a cyclonic gyre north of 12° N and an anticyclonic gyre south of it (Su, 2004). Embedded in the large gyres are many energetic mesoscale eddies observed by both hydrographic (e.g., Chu et al., 1998; Su et al., 1999) and satellite altimeter data (e.g., Shaw et al., 1999; Hwang et al., 2000; Wang et al., 2003; Chow et al., 2008). However, the eddy characteristics in the NSCS have not been well documented, especially these submesoscale eddies unresolved by SSHA. For example, what are their rotation periods? Do the cyclonic and anticyclonic exhibit distinct characteristics? Due to the dense sampling of satellite tracked drifters in the NSCS, this paper focuses on the eddy characteristics in the NSCS. The NSCS lies north of 16° N and is bordered by China, Vietnam, Taiwan Island, Luzon Island and Hainan Island (Fig. 2a), and is connected with Philippine Sea and East China Sea via the Luzon Strait and Taiwan Strait, respectively.

The paper is organized as follows. In Sect. 2 we introduce the drifter data and the method used to identify and characterize the eddies from drifter data. The eddy characteristics and important eddy statistics in the NSCS are described in Sect. 3. Finally, the paper concludes with a discussion in Sect. 4.

2 Data and eddy identification method

2.1 Data

The surface satellite-tracked drifters dataset spans from 1979 to the present and is part of the Global Drifter Program/Surface Velocity Program. The drifter has a spherical surface buoy and a semirigid drogue centered at 15 m depth that maintains its shape in high-shear flows. Once deployed, a modern drifter lives an average of around 400 days before ceasing transmission. Occasionally, drifters are picked up by fishermen or lose

OSD
8, 1575–1599, 2011

their drogue and run aground. The Atlantic Oceanographic and Meteorological Laboratory (AMOL) received the drifter positions from Doppler shift measurements from Service Argos. AOML's Drifter Data Assembly Center (DAC) assembles these raw drifter locations, applies quality control procedures, and interpolates them to regular 1/4-day intervals using an optimal interpolation procedure known as kriging (Hansen and Poulain, 1996). To remove high-frequency tidal and inertial wave energy and to avoid the energy into the low-frequency motions, these drifter data were daily averaged (Swenson and Niiler, 1996). The maximum amount of data was observed during the 1990s, corresponding to the World Ocean Circulation Experiment (WOCE) period.

In our study area, a total of 576 different drifters, able to exit and return to the area later (considered distinctly), were followed. Figure 2a shows all the drifter trajectories in the area and Fig. 2b shows the spatial distribution of the trajectories number. The number of drifter trajectories in the center of the study region is very big, whereas the regions near the coast of China and northwest of Luzon Island are poorly sampled.

2.2 Eddy identification method

Lagrangian drifters have been extensively utilized to track eddies, which are a reliable source of in-situ continuous data comparing with satellite remote sensing data. If the drifter is entrained into an eddy, it can exhibit the looping motion before being ejected. Eddies are thus revealed by clockwise and counterclockwise loops in drifter trajectories. The issue of identifying the coherent eddy structures in the drifter trajectories is then reduced to identifying the looping segments within a trajectory. Manual identification method for these loops from drifters has been conducted in many studies (e.g., Shoosmith et al., 2005; Chow et al., 2008). However, this is time-consuming and possibly subject to human error or bias. To identify these loops automatically, we developed an identification method based on the geometry of the drifter trajectory. This method is different from the geometric method of Boebel et al. (2003), which uses trajectory curvature to identify loops. Our method is based on the definition of loop: a loop is a closed curve with its starting point overlapped by its ending point. Because the sample points

OSD
8, 1575–1599, 2011

within the drifter trajectory are discrete, the overlapping point is in fact the overlapping point between the two intersectant trajectory segments.

It should be noticed not all the detected overlapping points correspond to the loops, such as the points C and D in Fig. 3a, which are actually the overlapping points of different loops. These points are called "false overlapping points", while A and B in Fig. 3a are called "true overlapping points" corresponding to the loops. To avoid the disturbing of the false overlapping points, we need do the skip searching, not the "one by one" point searching. Take point A as an example: suppose A is the overlapping point between the two intersectant trajectory segments ($P(i)-P(i+1)$, $P(j)-P(j+1)$), then the subsequent searching should start at point $P(j+1)$ not point $P(i+1)$. This skip can detect the true overlapping points A and B while ignoring the false overlapping points C and D (see Fig. 3a). However, we have noticed that there may exist small internal loops inside the bigger loop (Fig. 3b), which is likely to indicate the smaller eddy disturbance embedded inside the bigger eddy. Thus before the skipping, the internal searching in the range of the detected bigger loop should be made. Figure 3b shows a smaller loop identified inside the bigger one.

When the true overlapping points are detected, the sample points between the two intersectant lines are the whole loop points. One example showing the detected loops in a complex drifter trajectory is in Fig. 4.

The polarity of a loop is defined as the rotating direction of the loop. In Northern Hemisphere, when a drifter is caught by a cyclone (anticyclone) eddy, it will make the counter-clockwise (clockwise) loop. The situation is just converse in the Southern Hemisphere. Inspired by Sadarjoen and Post (2000) on a swirling pattern around a central set of points in the streamlines, we calculate the winding angle of the loop trajectory to determine the polarity of a loop (see more detail in Sadarjoen and Post, 2000). Figures 3 and 4 show the determined polarities of the detected loops.

The loop center can be estimated by geometrically averaging all the sample points contained in the loop. Here we define the loop radius (R) as the average distance among the distances between the loop points to the loop center. The rotating period

OSD
8, 1575–1599, 2011

(T_d) of a loop is defined as the time between the starting time and the ending time of the loop segment along the drifter sampling time series. Loop angle speed (L_a) can be calculated using the formula $L_a = 2\pi/T_d$, and the tangential speed (L_s) is $L_s = L_a \times R$.

During the movement of a drifter, if it is caught by an eddy for some time, it is possible the drifter can spin several times following the eddy (see Fig. 5). After extracting all the loops along a drifter trajectory, we can group the loops which are likely to represent the same eddy.

Rather than clustering loops, it is easier to cluster the center points. These center points are clustered as follows: the first point is considered as the first cluster. For each subsequent loop, if its polarity is the same with the first one, then we compute the distance between the center of the first loop and that of the subsequent loop. If the distance is less than the sum of the radii of the two loops, we group the subsequent loop to the first cluster. If the distance is bigger than the sum, the subsequent point constitutes a new cluster. After repeating the procedure among all the extracted loops within a drifter trajectory, the loops are combined into a distinct number of groups. Loops of the same group are considered as part of the same eddy. The number of loops representing the same eddy within a drifter trajectory suggests the circumrotating times of the drifter following an eddy.

3 Eddy characteristics and statistics in the NSCS

3.1 Mean flow

The Eulerian mean flow of NSCS was derived by spatially averaging the current components from the drifters in bins with $0.25^\circ \times 0.25^\circ$ (Fig. 6). The general pattern of mean flow is cyclonic, and there is an anticyclonic loop pattern within the Luzon Strait, indicating the Kuroshio occasionally makes a loop in this deep gap of western boundary (Shaw et al., 1999; Qu, 2000).

OSD
8, 1575–1599, 2011

3.2 Number and radii of eddies

The total number of the detected loops is 4360 (3532 anticyclonic, 828 cyclonic). After clustering the loops, there are 1972 eddies identified, in which 1599 are anticyclonic eddies and 373 are cyclonic eddies (Fig. 7a). Figure 8 shows the histogram of eddy radii with a bin width of 10 km. Note that due to the clarity of histogram, the radii less than 10 km are not plotted, because the numbers of these submesoscale eddies are 1466 and 253 for anticyclonic and cyclonic eddies, respectively, much bigger than the numbers of other scale eddies (Fig. 7b). Thus the drifter measurements have the ability to characterize the submesoscale eddies unresolved by satellite data. The mean radii of all the eddies, the cyclonic eddies and anticyclonic eddies are 3.5 km, 2.4 km and 4.7 km, respectively. If the submesoscale eddies (radius < 10 km) are ignored, the mean radii are 30.4 km, 31.7 km and 29.3 km for all the eddies, cyclonic and anticyclonic eddies, respectively. It should be pointed out the eddy sizes calculated from drifters are often underestimated because the drifter may be controlled by one part of an eddy (see Fig. 5). If we consider the drifters are on average statistically evenly distributed along the radius of eddy radius R, the probability density $p(r,\theta)$ of finding the drifter at a radius r and direction θ relative to the eddy center is constant (Chaigneau and Pizarro, 2005):

$$p(r,\theta) = \frac{1}{\int_0^R \int_0^{2\pi} r\,dr\,d\theta} = \frac{1}{\pi R^2} \tag{1}$$

The mean distance $\overline{R_1}$, or the expection

$$E(r) = \int_0^R \int_0^{2\pi} r^2 p(r,\theta)\,dr\,d\theta \tag{2}$$

OSD
8, 1575–1599, 2011

of the drifter from the eddy center is equal to $\overline{R_1} = 2R/3$. According to this formula, the mean eddy diameter of 7 km in the NSCS implies a characteristic eddy diameter of 10 km. This order of magnitude is smaller than the Rossby radii (50–90 km) of deformation in the SCS (Chelton et al., 1998).

According to the magnitude of eddy radii, the eddies can be categorized into three types: large eddies (radius > 60 km), median eddies (60 km ≥ radius ≥ 10 km) and small (or submesoscale) eddies (radius < 10 km). As for cyclonic (anticyclonic) eddies, the numbers of large, median and small types of eddies are 22 (10), 98 (123), 253 (1466), respectively. Wang et al. (2003) examined 7 years (1993–2000) SSHA data in this region, and also found more anticyclonic eddies than cyclonic eddies. It should be noted that the number of anticyclonic eddies detected from drifters is bigger than the eddies identified from SSHA. The reason may be that drifters are biased toward regions of convergent flow associated with anticylones (Chaigneau and Pizarro, 2005).

3.3 Spatial distribution of eddies

The spatial distribution of cyclonic and anticyclonic eddies from drifters in the NSCS is shown in Fig. 9. We follow Wang et al.'s geographical delineation of the zones based on the limited knowledge of the eddy generation mechanisms: Zone Z1 (southwest of Taiwan) and Zone Z2 (northwest of Luzon extending west to the 1000 m bath). In Zone Z1, more anticyclonic eddies are found, especially small-scale anticyclonic eddies are dominant. Wang et al. also found the same distribution pattern that anticyclonic eddies of small radius and short lifetime are dominant than cyclonic eddies in Z1. In Zone Z2, cyclonic eddies detected from drifter data are a little more than anticyclonic eddies, especially in the southeast of Hainan Island (Fig. 9), while SSHA data shows that anticyclonic eddies are a little more than cyclonic eddies in Z2 (Wang et al., 2003). But both data indicate the numbers of both types of eddies are the same order of magnitude. The small discrepancy may be because Wang et al. 's criterions used for identifying eddies from SSHA data are too strict, such as that the sea level difference

OSD
8, 1575–1599, 2011

between the outermost and the center of an eddy must be > 7.5 cm for at least a month. Some cyclonic eddies in Z2 may have not met that criterion, thus they are missed in Wang et al.'s results. Another possible reason is that the eddies detected from drifters not only contain mesoscale eddies resolved by SSHA but also submesoscale eddies unresolved by SSHA.

3.4 Temporal distribution of eddies

The temporal distribution of the total eddy number in 1979–2010 in the NSCS shows that the number of eddies peaks in the period of from May to July (Fig. 10a). However, if the eddies which radii are less than 10 km were eliminated, the distribution shows an opposite scene: the number of eddies peaks in the period from November to February of next year, while weaken in the period of from April to September (Fig. 10b).

SSHA data also indicates that more eddies generate during the winter monsoon (defined as from October to March of next year) in the NSCS, while less eddies generate during the spring transition period (April and May) and autumn transition period (September) (Wang et al., 2003). This temporal distribution pattern may be related to eddy generation mechanisms. During the winter monsoon, frontal instability at the Kuroshio intrusion could be one mechanism in shedding eddies in Z1 (Su et al., 2004). The orographic wind jets associated with the northeast winter monsoon and the gaps in the mountainous island chain along the eastern boundary of SCS can spin up cyclonic and anticyclonic eddies in Z2 (Wang et al., 2008).

But why does the temporal distribution of the total number of the eddies peak in summer when considering the submesoscale eddies? This may be ascribed to the great number of submesoscale eddies which are likely to generate in this period but seldom in the winter monsoon. These results suggest that the submesoscale eddies in the NSCS may not directly related to the upper ocean Ekman response to the wind, but may be related to the process of baroclinic instability (Wang G. H., personal communication). The background mechanism needs to be further studied.

OSD
8, 1575–1599, 2011

3.5 Tangential velocities of eddies

The relationship between period and radius of eddies is shown in Fig. 11. There is a significant correlation for both the cyclonic and anticyclonic eddies with orbital period increasing with eddy radius. Anticyclonic eddies increase a little more rapidly than cyclonic eddies, which could mean that cyclones tend to rotate more slowly than anticyclones in the NSCS. This can be validated further in Fig. 12 that shows the scatterplot of eddy radius and tangential velocity for cyclones and anticyclones. We can see that the maximum and mean tangential velocity of anticyclones is about 45 cm s^{-1} and 30 cm s^{-1}, respectively. In contrast, the two values are about 30 cm s^{-1} and 20 cm s^{-1} for cyclones, respectively. If the center of an eddy is in near-solid-body rotation, the period remains constant for increasing radii up to the position of the maximum tangential velocity. Therefore, we can speculate that drifters entrained into cyclones or anticyclones orbits at distances greater than the maximum tangential velocity.

The reconstructed tangential velocity as a function of eddy radius from all the identified eddies allows us to determine the normalized vorticity of the surface flow (Pingree et al., 1992; Aken et al., 2002; Chaigneau et al., 2005):

$$\left|\frac{\xi}{f}\right| = \left|\frac{1}{fr}\right| \left|\frac{\partial(rV_t)}{\partial r}\right| \tag{3}$$

where, ξ is the relative vorticity, f is the planetary vorticity, r is the distance to eddy center and V_t is the tangential velocity. At the radius 80 km, $\left|\xi/f\right|$ amounts to 0.07 (0.05) for anticyclones (cyclones), the magnitude increasing to 0.8 (0.6) for anticyclones (cyclones) within a radius of 10 km (the maximum V_t), while near the center $\left|\xi/f\right|$ is about 0.4 (0.3) for anticyclones (cyclones). These suggest the edges of large eddies are geostrophic balance, while the cores of large eddy are ageostrophic. In contrast, submesoscale eddies are ageostrophic from eddy edges to eddy cores. These results suggest that although the large-scale eddies may be considered in geostrophic balance, ageostrophic dynamics and centrifugal effects may play an important role in the growth, drift, and decay of the submesoscale eddies in the NSCS.

OSD
8, 1575–1599, 2011

4 Discussion and conclusions

On the basis of satellite tracked drifter measurements, eddies characteristics in the NSCS were generally investigated, especially these submesoscale eddies unresolved by SSHA. There are totally 1972 eddies identified, 4/5 of which are anticyclonic eddies. The spatial distribution of eddies are: in Zone Z1, the number of anticyclones dominate the number of cyclones, most of which are the submesoscale anticyclonic eddies with small radii; whereas, in Zone Z2, cyclonic eddies are a little more than anticyclonic eddies. We also notice that if the submesoscale eddies are eliminated, then the eddies in the NSCS will show a 1.1–1 dominance with the number (133) of anticyclones over the number (122) of cyclones. It is a very interesting topic to analyze these submesoscale eddies, such as their generation mechanisms and their role in the water exchange of Luzon Strait. But this is beyond the scope of the paper.

The temporal distribution of eddy number from drifter in the NSCS has a close relation with monsoon. The number of eddies (submesoscale eddies ignored) peak during the winter monsoon, while eddies tend to decrease quickly in the transition periods of monsoon. The spatial and temporal patterns have a good agreement with the results of SSHA. This may validate the suitability of our identification method. Meanwhile, the submesoscale eddies are likely to generate in the summer monsoon but seldom in the winter monsoon, which may be related to the baroclinic instability.

The maximum and mean tangential velocities of anticyclones (cyclones) is 45 (30) cm s^{-1} and 30 (15) cm s^{-1}, respectively. It may indicate that anticyclones tend to rotate more quickly than cyclones in the NSCS. The normalized vorticity $|\xi/f|$ calculated from all the identified eddies suggest that large-scale eddies are in geostrophic balance, but ageostrophic dynamics may be important for the submesoscale eddies where centrifugal effects cannot be ignored.

In addition, this study may be complementary to studies based on altimeter data in the NSCS. Their combined use is expected to achieve a more complete view of ocean dynamics in the NSCS. This work may also provide useful information for the choice

OSD
8, 1575–1599, 2011

of appropriate spatial resolution of these eddy-resolving models along with developing strategies on future drifter deployments in the NSCS.

Acknowledgements. The drifter data were provided by the National Oceanic and Atmospheric Administration (NOAA). This work was supported by National Natural Science Foundation of China (Grants Nos. 41176085 and 41075045). Helpful comments by Wang G. H. are gratefully acknowledged.

References

Aken, H. M. v.: Surface currents in the Bay of Biscay as observed with drifters between 1995 and 1999, Deep-Sea Res. Pt. I, 49, 1071–1086, 2002.

Boebel, O., Lutjeharms, J., Schmid, C., Zenk, W., Rossby, T., and Barron, C.: The cape cauldron: a regime of turbulent inter-ocean exchange, Deep-Sea Res. Pt. II, 50, 57–86, 2003.

Chaigneau, A. and Pizarro, O.: Eddy characteistics in the Eastern South Pacific, J. Geophys. Res., 110, C06005, doi:10.1029/2004JC002815, 2005.

Chelton, D. B., Deszoeke, R. A., and Schlax, M. G.: Geographical variability of the first baroclinic Rossby radius of deformation, J. Phys. Oceanogr., 28, 433–460, 1998.

Chow, C.-H., Hu, J.-H., Centurioni, L. R., and Niiler, P. P.: Mesoscale Dongsha cyclonic eddy in the Northern South China Sea by drifter and satellite observations, J. Geophys. Res., 113, C04018, doi:10.1029/2007JC004542, 2008.

Chu, P. C., Fan, C. W., Lozano, C. J., and Kerling, J. L.: An airborne expendable bathythermograph survey of the South China Sea, May 1995, J. Geophys. Res., 103(C10), 21637–21652, 1998.

Hansen, D. V. and Poulain, P.-M.: Quality control and interpolations of WOCE-TOGA drifter data, J. Atmos. Ocean. Tech., 13, 900–909, 1996.

Hwang, C.: Circulations and eddies over the South China Sea derived from TOPEX/Poseidon altimetry, J. Geophys. Res., 105(C10), 23943–23965, doi:10.1029/2000JC900092, 2000.

Pingree, R. D. and Cann, B. L.: Three anti-cyclonic slope water oceanic eDDIES (SWODDIES) in the Southern Bay of Biscay in 1990, Deep-Sea Res. Pt. I, 39, 1147–1175, 1992.

Qu, T. D.: Upper-layer circulation in the South China Sea, J. Phys. Oceanogr., 30, 1450–1460, 2000.

OSD

8, 1575–1599, 2011

Sadarjoen, I. A. and Post, F. H.: Detection, quantification, and tracking of vortices using streamline geometry, Comp. Graph., 24, 333–341, 2000.
Shaw, P. T., Chao, S. Y., and Fu, L.: Sea surface height variations in the South China Sea from satellite altimetry, Oceanol. Acta, 22(1), 1–17, 1999.
Shoosmith, D. R., Richardson, P. L., Bower, A. S., and Rossby, H. T.: Discrete eddies in the Northern North Atlantic as observed by looping RAFOS floats, Deep-Sea Res. Pt. II, 52, 637–650, 2005.
Su, J. L.: Overview of the South China Sea circulation and its influence on the coastal physical oceanography outside the Pearl River Estuary, Cont. Shelf. Res., 24, 1745–1760, 2004.
Su, J. L., Xu, J. P., Cai, S. Q., and Wang, O.: Gyres and eddies in the South China Sea, onset and evolution of the South China Sea monsoon and its interaction with the ocean, edited by: Yihui, D. and Chongyin, L., China Meteorological Press, Beijing, China, 272–279, 1999. (in Chinese)
Swenson, M. S. and Niiler, P. P.: Statistical analysis of the surface circulation of the California Current, J. Geophys. Res., 101(C10), 22631–22645, 1996.
Wang, G. H., Su, J. L., and Chu, P. C.: Mesoscale eddies in the South China Sea observed with altimeter data, Geophys. Res. Lett., 30, 2121, doi:10.1029/2003GL018532, 2003.
Wang, G. H., Chen, D. K., and Su, J. L.: Winter eddy genesis in the Eastern South China Sea due to orographic wind jets, J. Phys. Oceanogr., 38, 726–732, 2008.

OSD
8, 1575–1599, 2011

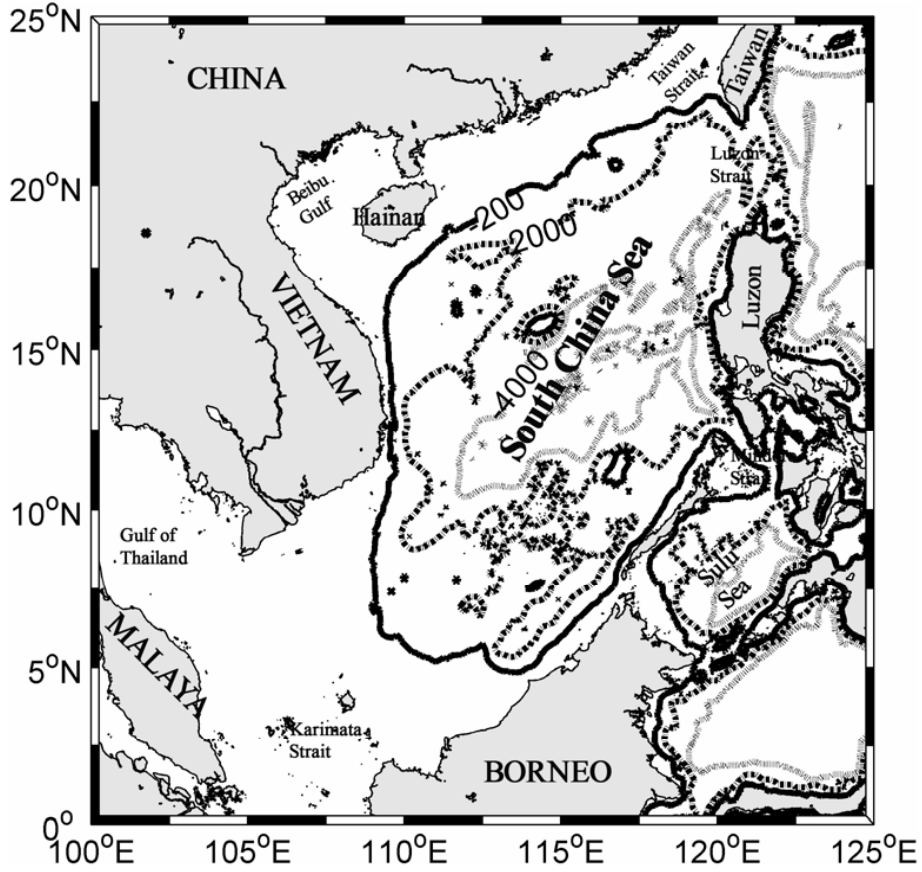

Fig. 1. Bathymetry of the SCS, with only −200 m, −2000 m, and −4000 m contours plotted.

OSD
8, 1575–1599, 2011

Eddy characteristics in the NSCS from drifter

J. Li et al.

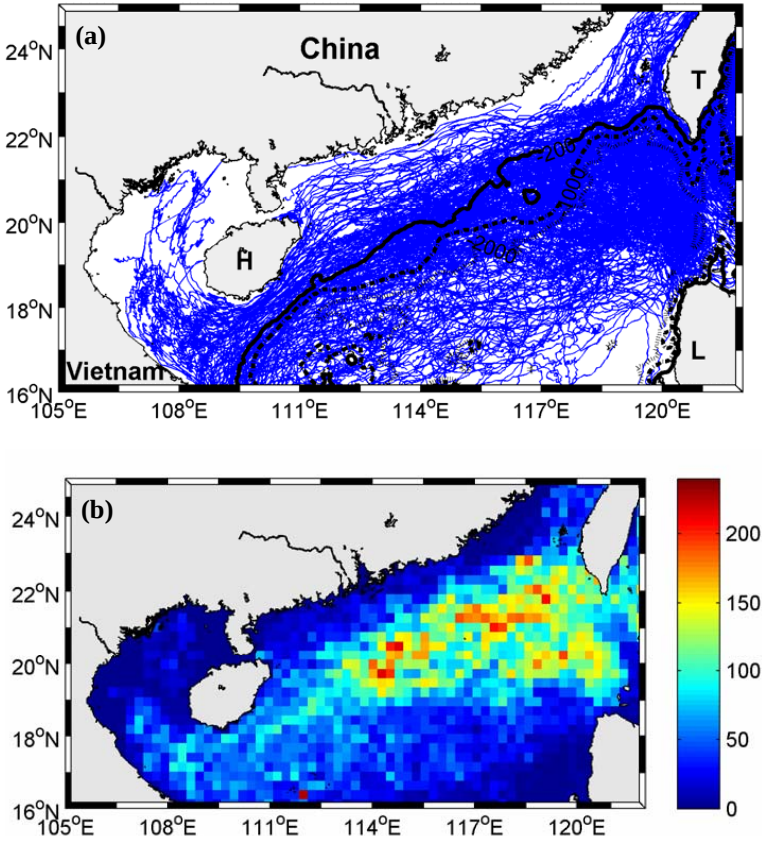

Fig. 2. **(a)** All the 576 drifter trajectories in the NSCS from 1979 to March 2010 in the study region (105°–122° E, 16°–25° N). Isobaths are in meter. H: Hainan Island. T: Taiwan Island. L: Luzon Island. **(b)** Drifter trajectory number in bins with 0.25° × 0.25°.

OSD
8, 1575–1599, 2011

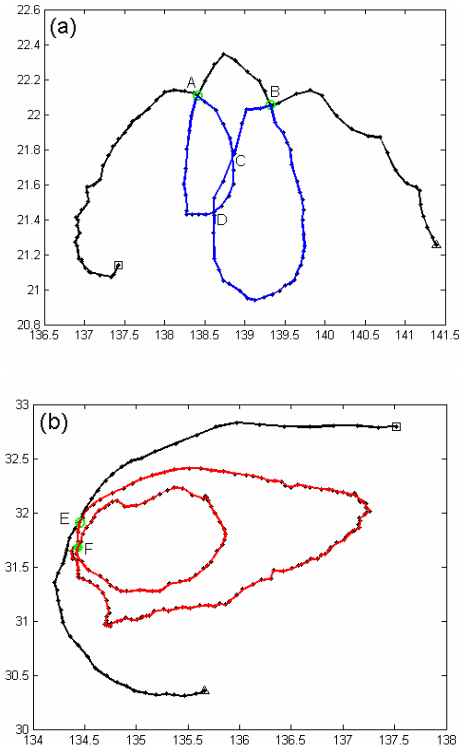

Fig. 3. (a) An example of loops identified in drifter trajectory shown with the solid line. The solid points represent the sample points along the drifter trajectory. The starting point and ending point of this trajectory is marked with triangle and square, respectively. The green empty circles are the true overlapping points marked with A and B, while the false are marked with C and D. **(b)** An example of a bigger loop containing a smaller loop identified. The green empty circle E is the overlapping point of the bigger loop, and the green solid circle F represents the overlapping point of the internal smaller loop. The blue (red) segments are indicated as counter-clockwise (clockwise) loops.

OSD
8, 1575–1599, 2011

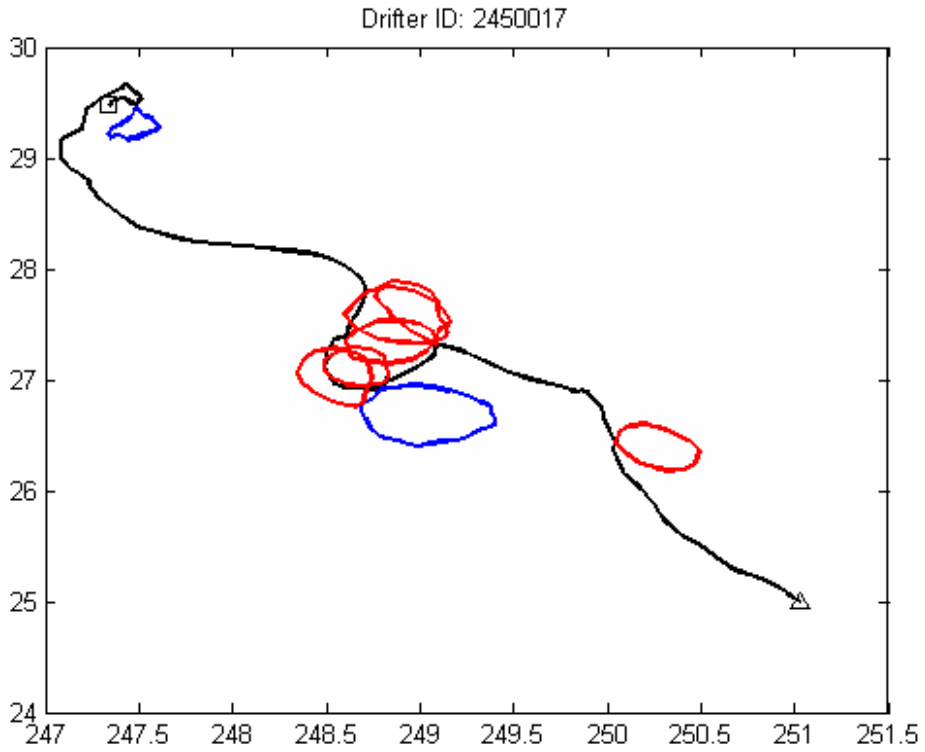

Fig. 4. An example showing the complexity of a realistic drifter trajectory. The blue (red) segments are indicated as counter-clockwise (clockwise) loops. The starting point and ending point of this trajectory is marked with triangle and square, respectively.

OSD
8, 1575–1599, 2011

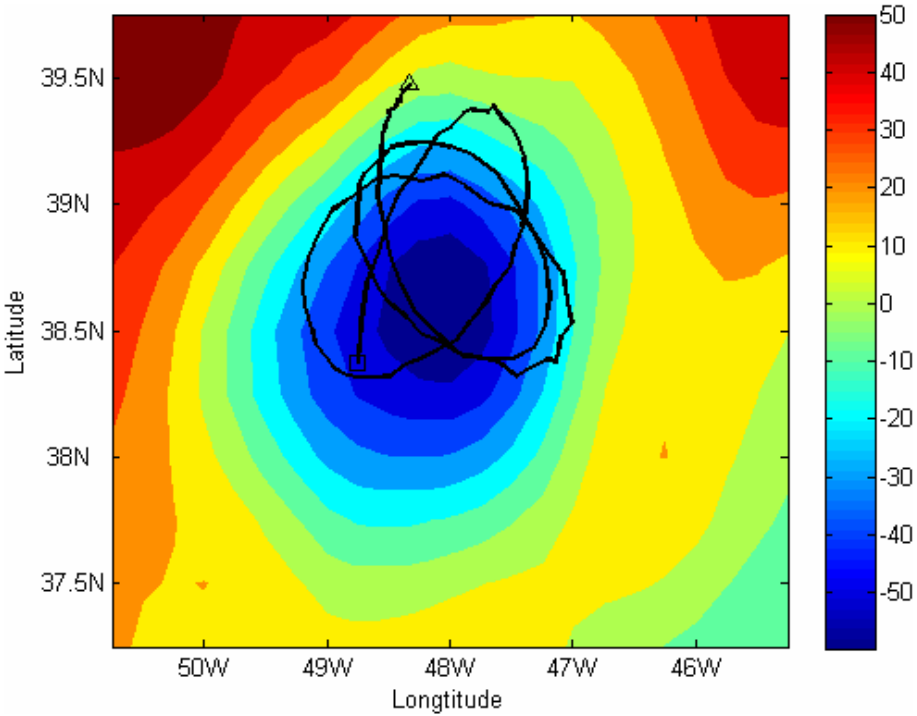

Fig. 5. An example of one drifter (ID: 78922) circumrotating three times when caught by an cyclonic eddy. Black curve is the drifter trajectory, and the starting point and ending point of this trajectory is marked with triangle and square, respectively. Colorful filled contours show the SSHA data in 10 September 2008, corresponding to the drifter sampling.

OSD
8, 1575–1599, 2011

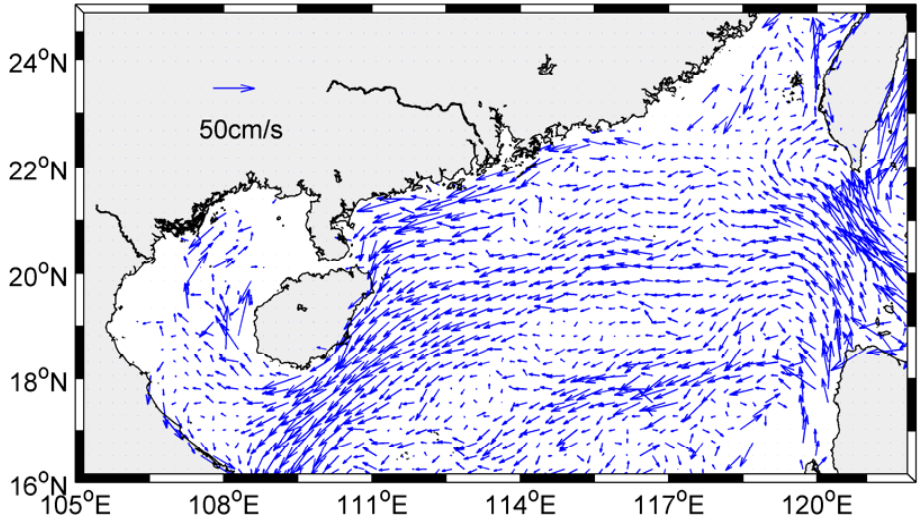

Fig. 6. Mean flow in the NSCS from averaging all the drifter trajectories.

OSD
8, 1575–1599, 2011

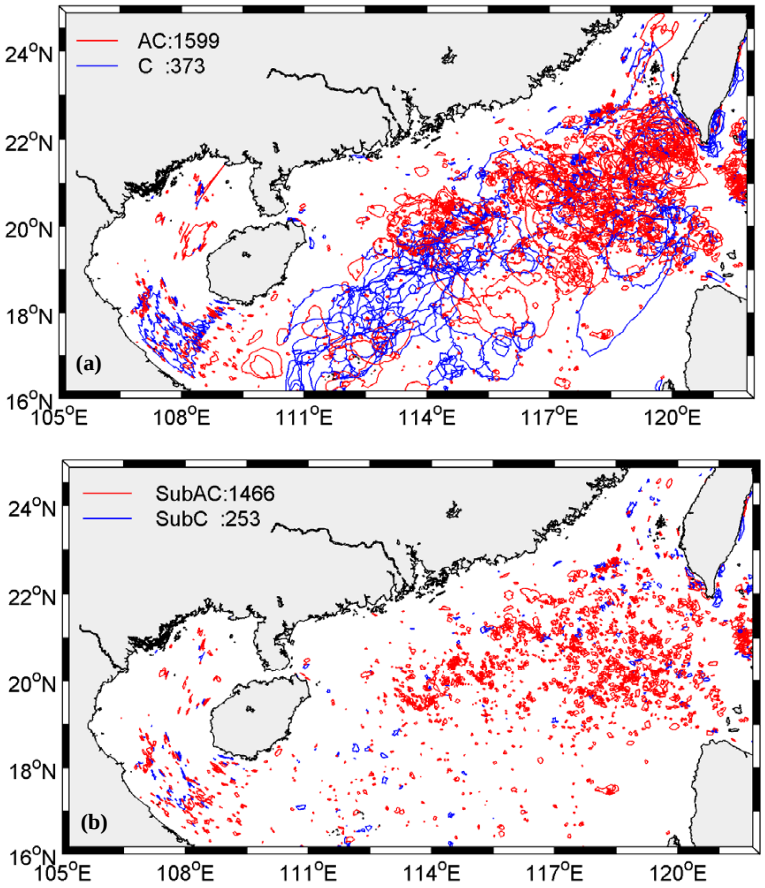

Fig. 7. **(a)** Anticyclonic (red) and cyclonic (blue) eddies detected from drifer trajectories in the NSCS. **(b)** As in **(a)**, but for submesoscale anticyclonic (red) and cyclonic (blue) eddies which radii are less than 10 km.

OSD
8, 1575–1599, 2011

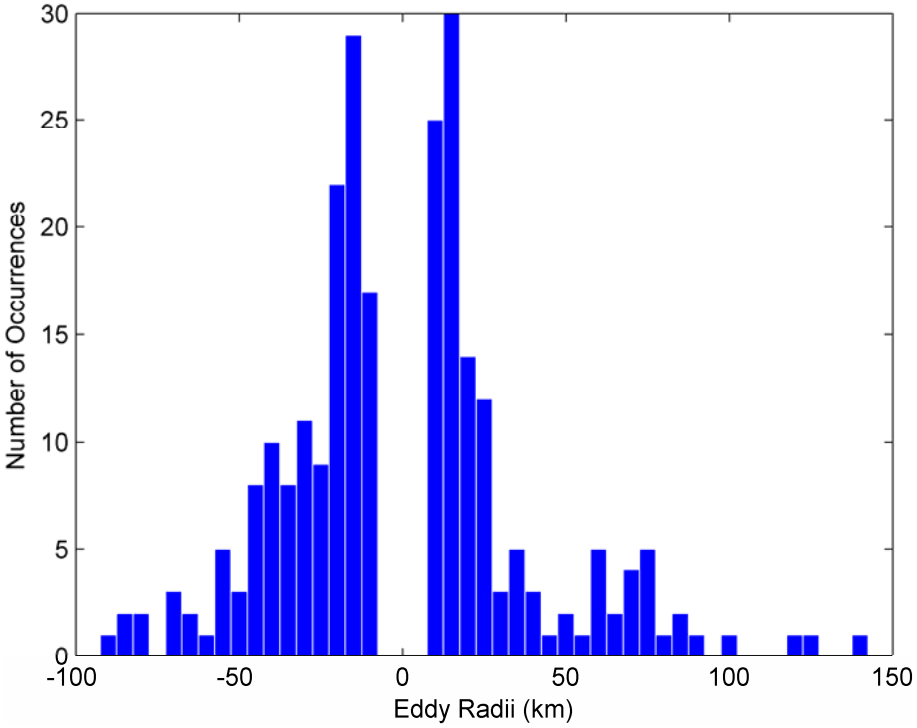

Fig. 8. Histogram of eddy radii with a bin width of 10 km. Positive radii depict cyclonic eddies, and negative radii depict anticyclonic eddies.

OSD
8, 1575–1599, 2011

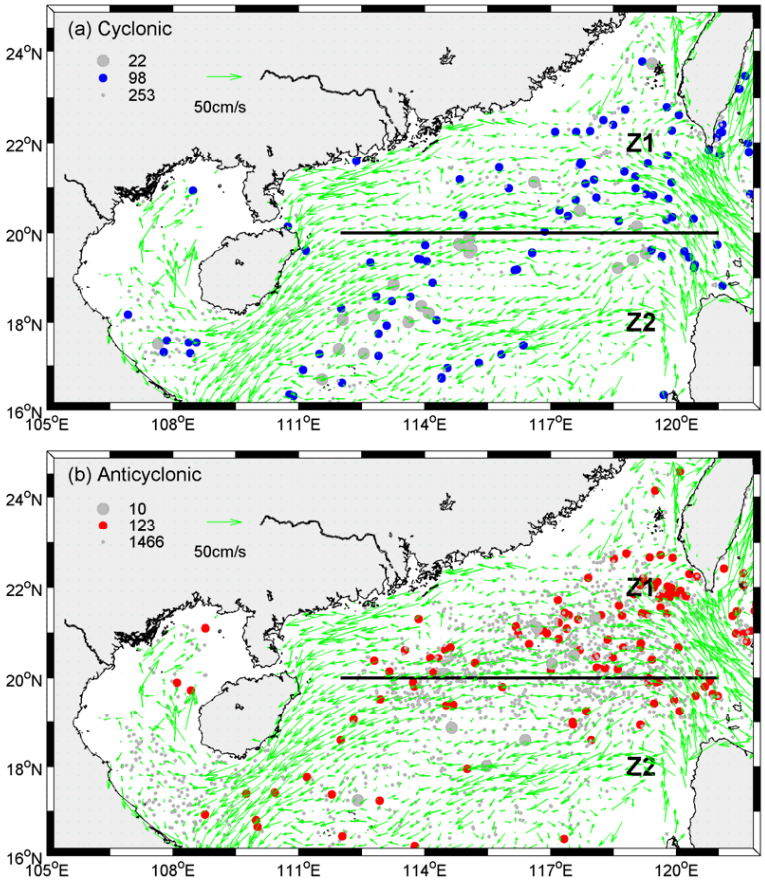

Fig. 9. The distribution of cyclonic **(a)** and anticyclonic **(b)** eddies detected from drifters in the NSCS. Large eddies are shown by the big gray solid dots, median eddies are shown by the middle solid dots (blue: cyclone, red: anticyclone), and small eddies are shown by the small gray solid dots.

OSD
8, 1575–1599, 2011

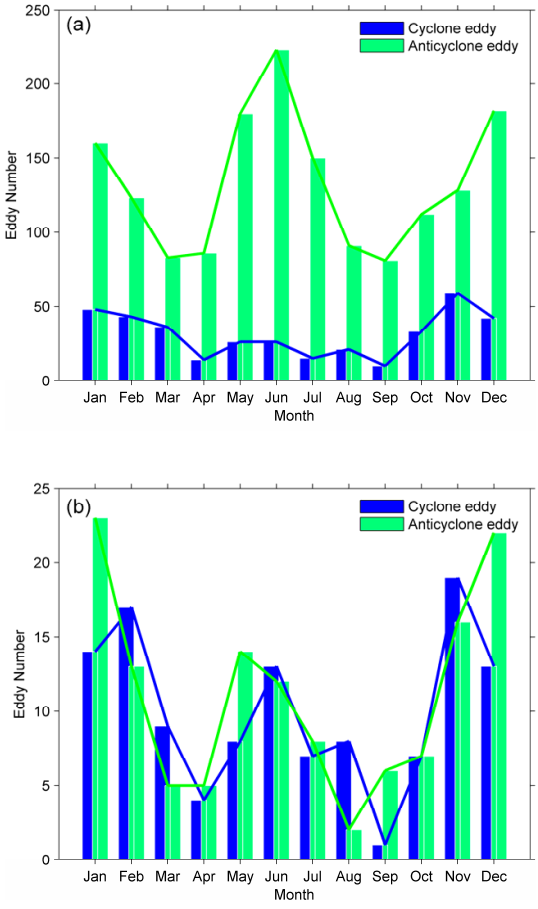

Fig. 10. (a) The total number of eddies (1979–2010) as a function of the month of the year for cyclonic eddies (blue) and anticyclonic eddies (green). **(b)** As in **(a)**, but for eddies which radii are > 10 km.

OSD
8, 1575–1599, 2011

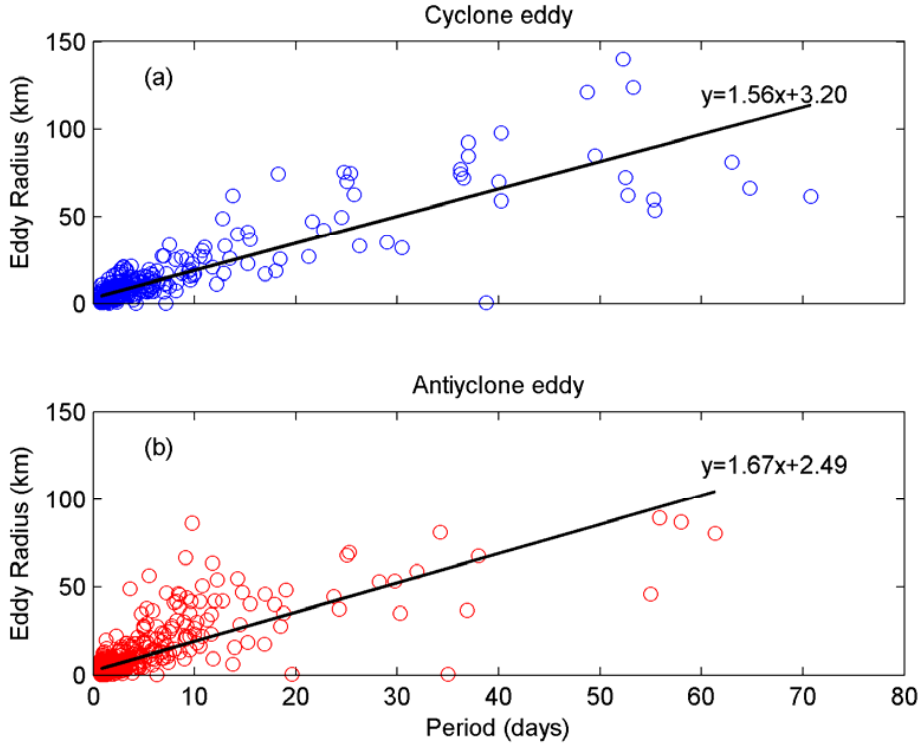

Fig. 11. Scatterplot of eddy radius and period for cyclones **(a)** and anticyclones **(b)**.

OSD
8, 1575–1599, 2011

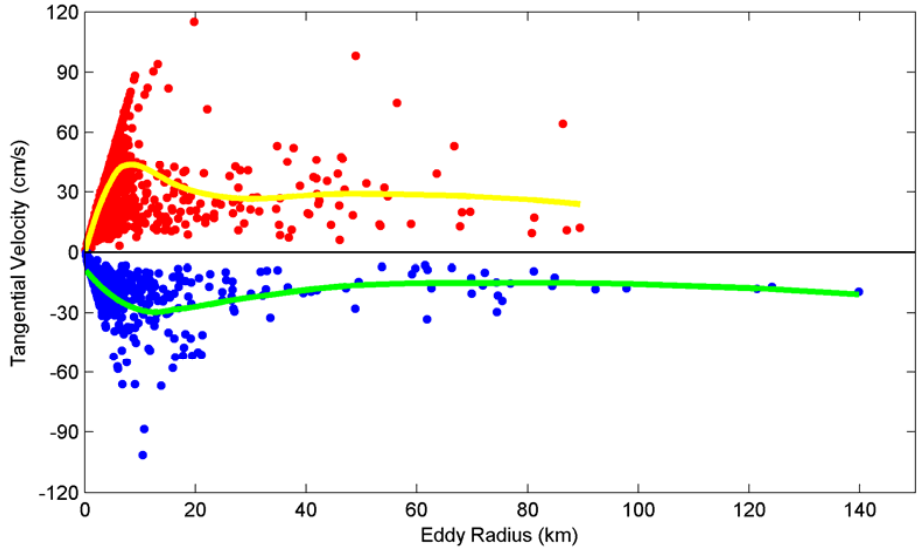

Fig. 12. Scatterplot of eddy radius and tangential velocity for cyclones (blue) and anticyclones (red).

OSD
8, 1575–1599, 2011